HHS Public Access

Author manuscript

Comput Med Imaging Graph. Author manuscript; available in PMC 2024 January 22.

Published in final edited form as:

Comput Med Imaging Graph. 2022 July ; 99: 102076. doi:10.1016/j.compmedimag.2022.102076.

Using Temporal and Structural Data to Reconstruct 3D Cerebral Vasculature from a Pair of 2D Digital Subtraction Angiography Sequences

Sarah Frisken[*,1,3], **Nazim Haouchine**[1,3], **Rose Du**[1,2,3], **Alexandra J. Golby**[1,2,3]

[1.] Department of Radiology, Brigham and Women's Hospital

[2.] Department of Neurosurgery, Brigham and Women's Hospital

[3.] Harvard Medical School

Abstract

Purpose: The purpose of this work is to present a new method for reconstructing patient-specific three-dimensional (3D) vasculature of the brain from a pair of digital subtraction angiography (DSA) image sequences from different viewpoints, e.g., from bi-plane angiography. Our long-term goal is to provide high resolution visualization of 3D vasculature with dynamic flow of contrast agent from limited data that is readily available during surgical procedures. The proposed method is the second of a three-stage process composed of 1) augmenting vessel segmentation with vessel radii and timing of the arrival of a bolus of contrast agent, 2) reconstructing a volumetric representation of the augmented vessel data from the augmented 2D segmentations, and 3) generating a 3D model of vessels and flow of contrast agent from the volumetric reconstruction. Unlike previous methods, which are either limited to relatively simple vessel structures or rely on multiple views and/or prior models of the vasculature, our method requires only a single pair of 2D DSA sequences taken from different view directions.

Methods: We developed a new mathematical algorithm that augments vessel centerlines with vessel radii and bolus arrival times derived directly from the 2D DSA sequences to constrain the 3D reconstruction. We validated this method on digital phantoms derived from clinical data and from fractal models of branching tree structures.

Results: In standard reconstruction methods, reconstruction by projection of two views into 3D space results in 'ghosting' artifacts, i.e., false 3D structure that occurs where vessels or vessel segments overlap in the 2D images. For the complex vascular of the brain, this ghosting is severe and is a major hurdle for methods that attempt to generate 3D structure from 2D images. We show that our approach reduces ghosting by up to 99% in digital phantoms derived from clinical data.

Conclusion: Our dramatic reduction in ghosting artifacts in 3D reconstructions from a pair of 2D image sequences is an important step towards generating high resolution 3D vasculature with dynamic flow information from a single DSA sequence acquired using bi-plane angiography.

[*]Corresponding author, sfrisken@bwh.harvard.edu.

Keywords

3D reconstruction; brain blood vessels; cerebral vasculature; digital subtraction angiography

1. Introduction

We present a new method for reconstructing three-dimensional (3D) image volumes of the brain vasculature from two-dimensional (2D) angiography. The method reconstructs 3D images from two 2D digital subtraction angiograph (DSA) sequences. Such sequences can be acquired on commercial biplane angiography systems that are commonly available in interventional radiology suites. This work is motivated by the goal of providing high resolution patient-specific models of 3D vessel structure in the brain and visualization of flow through these models to help neurosurgeons and neuroradiologists plan and monitor neurosurgical interventions.

Understanding patient-specific cerebral vasculature is important for several neurological disorders including intracranial aneurysms, arteriovenous fistulae, arteriovenous malformations, highly vascularized tumors and stroke, and for accessing lesions near the skull base where the vasculature is variable and complex. Our research focuses on image-guided planning for surgery of cerebral arteriovenous malformations (AVMs), where a complete understanding of the vasculature near the nidus of the AVM, i.e., the feeding, draining and *en passage* vessels, can help reduce surgical complications (Benes and Bradáč, 2017; Lawton and Lang, 2019; Rolston et al., 2013; Vassallo et al., 2018). Specifically, when surgically removing an AVM, the surgeon must ligate feeding vessels before draining vessels to avoid hemorrhage of the AVM and should avoid clipping *en passage* vessels to prevent inadvertent damage to healthy brain tissue (Kalani and Yashar, 2015). However, the cerebral vasculature is highly complex, particularly near the nidus of the AVM, and important feeding or *en passage* vessels may be too small to be resolved with conventional 3D imaging and it may be obscured in 2D images by tortuous vessels and overlapping circulations.

2D DSA is the gold standard for planning and monitoring surgical and endovascular interventions for cerebrovascular disorders (Benes and Bradáč, 2017). In DSA, a pre-contrast reference x-ray is recorded. A bolus of contrast agent is then injected intra-arterially and a time sequence of x-rays is acquired. The reference image is subtracted from each x-ray to generate a sequence of images showing the contrast agent moving through the vessels (Fig. 1). DSA images have high spatial resolution (0.08 mm x 0.08 mm to 0.2 mm x 0.2 mm pixels) and relatively high temporal resolution (typically 1–3 frames per second (fps) and up to 8–15 fps) (Ide et al., 2012; Zhang et al., 2016) and DSA is broadly available in interventional radiology suites (Çimen et al., 2016). In addition, contrast agent can be injected locally at controlled rates so that imaging can be focused on a sub-circulation of interest. However, DSA images are 2D so it can be challenging and time consuming for clinicians to interpret the subtleties of 3D blood flowing in and out of complex pathologies such as AVMs.

Tomographic imaging (e.g., magnetic resonance angiography (MRA) and computed tomography angiography (CTA)) are also commonly available clinically (Fig. 1). They can be visualized using direct volume rendering or 3D models of blood vessels in the brain. However, vessels less than 1mm in diameter cannot be easily resolved and these methods do not provide information about blood flow (Zhang et al., 2016). Dynamic CTA (Matsumoto et al., 2007) and dynamic MRA (Gauvrit et al., 2005; Griffiths et al., 2000; Tsuchiya et al., 2000; Ziyeh et al., 2005) provide some information about 3D blood flow, but at much lower spatial and temporal resolution that DSA. In addition, tomographic imaging is typically not available in the operating room for intraoperative imaging. 3D rotational DSA is acquired in a similar manner to 2D DSA and can often be acquired with the same device. After the bolus is injected and the vessels of interest have been fully infused with contrast agent the x-ray source and detector are rotated 180–240 degrees about the head while multiple (>100) 2D images are acquired. A tomographic image is then reconstructed to generate a 3D image of the vasculature at a single snapshot in time (e.g., typically at the end of arterial phase) with voxel sizes from 0.33 mm x 0.33 mm x 0.33 mm to 0.7 mm x 0.7 mm x 0.7 mm (Orth et al., 2008).

Our goal is to generate 3D images of cerebral vasculature with spatial and temporal resolutions approaching that of 2D DSA from a single pair of 2D DSA sequences acquired on a biplane angiography system. There has been much work in this area during the past 30 years (see, e.g., (Bullitt et al., 1997; Grist et al., 2012) for a history of vascular imaging), however, as discussed in a recent literature review (Çimen et al., 2016), there are still multiple challenges remaining.

1.1 Background

Much of the research in reconstructing 3D models of vasculature has been for imaging and modeling blood flow in the coronary arteries (Blondel et al., 2004; Cardenes et al., 2012; Chen et al., 2013; Fang et al., 2018; Galassi et al., 2018; Jandt et al., 2009; Liao et al., 2010; Merle et al., 1998; Oueslati et al., 2018; Tran, 2017; Vardhan et al., 2019; Zifan and Liatsis, 2016; Zifan et al., 2008) (see literature reviews in (Chen and Carroll, 2000; Çimen et al., 2016; Garcia, 2013)). Visualizing the main coronary arteries does not require sub-millimeter resolution and they are less complex than the tortuous vasculature of the brain. However, reconstruction of coronary arteries remains a challenging problem due to motion artifacts caused by breathing and the cardiac cycle which introduce non-rigid deformation during image acquisition. There has also been some work in visualizing and modeling 3D vasculature of the brain (Copeland et al., 2010; Spiegel et al., 2011; Wachter, 2009). Although cerebral vasculature imaging does not suffer from severe motion artifacts (assuming the patient can hold their head still for the 10 or more seconds required for image acquisition), small vessels or small vessel features (e.g., aneurysms or stenosis) require sub-millimeter imaging. Additionally, the cerebral vasculature is complex, with dense, intertwining circulations and tortuous vessels that can overlap each other when projected onto 2D views and may run perpendicular to the viewing direction.

Related work in the field of computer vision reconstructs 3D shape from multiple 2D camera views or from video of moving objects. Some computer vision techniques are applicable

to reconstructing 3D vessels from 2D DSA images. For example, (Berthilsson and Astrom, 1997; Cai et al., 2011; Mai and Hung, 2010; Saini et al., 2015) reconstruct 3D curves from two or more 2D views and (Martin et al., 2014) reconstructs 3D structure of “jumbled” overlapping tubular objects from 2D video sequences.

There are two basic approaches for reconstructing 3D shape from 2D views: *volumetric reconstruction* and *model-based reconstruction*. 3D rotational DSA is a form of volumetric reconstruction. In volumetric reconstruction, multiple 2D images of the subject are taken at different viewing directions and the 2D views are back projected into 3D space and combined to generate a volumetric image. In the case of rotational DSA, 100’s of 2D projection images are acquired as the imaging device is rotated around the subject and a volumetric image of the vasculature is reconstructed from the 2D projections using cone-beam back projection (Feldkamp et al., 1984). The use of contrast agent and subtraction of a pre-contrast image combined with a relative sparsity of contrast-enhanced vessels in DSA can support volumetric reconstruction from fewer 2D DSA images when the vasculature is not too complex (Copeland et al., 2010; Jandt et al., 2009). These methods filter the 2D images to enhance vessels and further reduce background noise (e.g., using (Frangi et al., 1998)), back project the filtered images into 3D and combine the back projected image values to generate a *vesselness* value for each voxel in the 3D image volume. These values can be directly rendered using volume rendering or further processed to generate models of the vasculature. In contrast, model-based reconstruction methods process the 2D images to generate 2D models of blood vessels in the form of vessel centerlines (which can be represented as points, connected points or curve segments) and/or a vessel tree composed of vessel end and branching points connected by vessel segments. Processing steps include filtering to enhance vessels, vessel segmentation, and centerline/model extraction. These 2D models of the vasculature are back projected into 3D space along x-ray projection lines (Fig. 2). Each model element (point, feature, centerline, etc.) from one view is matched with the most likely corresponding model elements of all other views. Triangulation of the back-projected coordinates of these matched elements is then used to determine the 3D coordinates of the most likely matched element. The matching can be constrained by vessel connectivity and the vessel tree structure. 2D segmentation, model construction and matching can each be done manually, semi-automatically or fully automatically.

Previous work can be further classified by the number of views used to reconstruct 3D vasculature and/or the use of auxiliary data such as a prior 3D model. Reconstruction from two 2D views has been limited to relatively simple vascular geometry, such as a single curved structures (e.g., a catheter in fluoroscopy images (Delmas et al., 2015)), isolated curve segments (Bullitt et al., 1997), or the main coronary arteries (Cardenes et al., 2012; Merle et al., 1998; Oueslati et al., 2018) which exhibit minimal self-overlapping given well-chosen view directions. These methods typically use model-based reconstruction and may require manual intervention to detect vessel endpoints and bifurcations. Most approaches have used 3 or more view directions (Blondel et al., 2004; Galassi et al., 2018; Henri and Peters, 1996; Lee et al., 2007; Li and Cohen, 2011; Liao et al., 2010; Tran, 2017). Henri *et al.* (Henri and Peters, 1996) used a model-based method to generate all possible matches from 2 views and then used a 3rd view and tree structure connectivity to narrow down possible matches. Most other approaches require 4 or more views (Galassi et al., 2018; Jandt

et al., 2009; Lee et al., 2007; Li and Cohen, 2011; Liao et al., 2010). Some authors have used 2D DSA to enhance an *a priori* 3D model generated from 3D imaging such as MRA, CTA or rotational DSA (Bullitt et al., 1997; Davis et al., 2013; Platzer et al., 2008; Schmitt et al., 2002; Spiegel et al., 2011; Wacker et al., 2008). This approach was first proposed by Bullit *et al.* (Bullitt et al., 1997) who used 2D DSA to add additional detail such as smaller vessels to the 3D model.

2D DSA has also been used to augment a priori 3D models with flow information (Copeland et al., 2010; Davis et al., 2013; Platzer et al., 2008; Schmitt et al., 2002). Copeland et al. (Copeland et al., 2010) projects a 2D DSA sequence into a 3D image to get a time sequence of 3D images. Schmitt et al. (Schmitt et al., 2002) and Davis et al. (Davis et al., 2013) constructed an a priori 3D model from MRA and projected timing data from the 2D DSA sequence onto the model to generate a visualization of flow. Platzer (Platzer et al., 2008) generated a 3D model of cerebral vasculature from a 3D MRA or CTA image and simulated flow using particle-based methods. The flow model is optimized iteratively by minimizing the difference between projections of the simulated flow and corresponding 2D DSA views. Wachter proposed a method to acquire both 3D geometry and timing by performing rotational angiography during the contrast injection rather than after the structures of interest have already been saturated (Wachter, 2009). However, this method requires a new image acquisition protocol and does not reconstruct small vessels or the venous phase.

2. Materials and methods

2.1 Approach

Unlike previous work, our goal is to reconstruct 3D vasculature from a single pair of 2D DSA sequences acquired simultaneously using a bi-plane scanner. Unlike previous methods which constrain reconstruction by assuming a simplified vessel structure or multiple views or a prior 3D model, we use timing information as the bolus advances through the vessels and vessel diameters to constrain the 3D reconstruction and disambiguate overlapping vessels. Our approach requires three stages: 1) 2D image processing; 2) constrained volumetric reconstruction; and 3) model construction, as illustrated in Fig 3. This paper presents a novel method for stage 2). We present our mathematical formulation, detailed methodology and validation on 3D phantom models. We use two types of digital phantoms for validation: synthetic fractal trees that have programmable branching complexity and a structure similar to that of cerebral vasculature circulations (Fig 4.); and 3D models of different circulations in the brain extracted from MRA images (Fig. 5).

For stage 2, we use the following steps:

1. Generate, for each 2D view, a synthetic annotated 2D image to represent the output of stage 1,
2. Reconstruct a volumetric representation of the vessel structure using our new method (stage 2), and

3. Visualizing the reconstructed volume using iso-surface rendering to analyze the reconstruction

Phantom model processing, computation of annotated images, 3D reconstruction and validation were implemented in a custom C^{++} application that was designed and implemented for this project.

2.2 Data Preparation and Processing

2.2.1 Phantom Models—We used two types of digital phantoms of 3D cerebral vasculature: fractal trees and models generated from MRA images of human brains. Fractals are frequently used to generate realistic trees for computer graphics and animation. We used a fractal tree generator in (Weber and Penn, 1995) to generate models that are similar in complexity and geometry to arteries in the brain. Using fractal trees allowed us to generate pseudo-random models with controlled parameters such as general tree shape, mean branch lengths and radii, and the number of levels of branching. This allowed us to test our system with controlled levels of model complexity. We used Arbaro (Diestel and Moeller, 2003–2012), an open source implementation of (Weber and Penn, 1995), with variations of their “desert-bush” with up to 3 levels of branching to generate our phantoms. Fig. 4 show examples of a fractal tree than we used to test our system.

As a second type of phantom, we used digital reconstructions of arterial trees from The Brain Vasculature (BraVa) database (http://cng.gmu.edu/brava, 2020). This database contains digital reconstructions of the human brain arterial trees from MRA images of 61 healthy adult subjects along with extracted morphological measurements including vessel radii. Each data set in the database includes 6 major circulations stemming from the Circle of Willis, including the left and right anterior cerebral arteries, middle cerebral arteries, and posterior cerebral arteries. Examples of vasculature that we reconstructed from this database are shown in Fig. 5.

For both phantom types, we represent models as a list of vessel centerlines represented as line segments, where each segment is augmented with a vessel radius that varies linearly along the segment. Each model contains a base node and a hierarchy of branches that form an acyclic graph. For simplicity, we assume that the contrast agent is injected at the base node and travels at a uniform speed in the 3D model until a branch tip is reached. Thus, bolus arrival time is zero at the base node and increases linearly with path length, where path length at a point on the centerline is the distance that the bolus would travel from the base node along the 3D model centerlines to reach that point. We note that this model of flow is deliberately simplistic; Accurate models of blood flow through the branching cerebral vessels as they narrow to the size of capillaries are not yet available. Fortunately, an accurate model of blood flow is not required by this algorithm which only requires that the arrival of the bolus of contrast agent at each point along each vessel is the same in both DSA image sequences. This is true in bi-plane scanners where the two images are acquired simultaneously with a single injection of contrast.

2.2.2 Image Annotation—As input to the second stage of our pipeline, we compute two 2D annotated images by projecting centerlines of each phantom model onto two orthogonal

views. The projection operation is based on a general cone-beam angiography system illustrated in Fig. 2 as described in (Chen et al., 2013; Jandt et al., 2009; Xiao et al., 2003). Our implementation can generate projections in arbitrary directions, but we chose to perform validations using front-to-back (*anterior-posterior*) and left-to-right or right-to-left (*lateral*) view directions. Although view directions could be optimized to reduce self-inclusions (perhaps depending on the arterial tree of interest or patient anatomy), we opted to use the standard clinical anterior-posterior and lateral views to ensure 1) that we will have sufficient retrospective data for next-step machine-learning automation of the annotated segmentation and bolus arrival time detection, and 2) that our method will work for current clinical practice, thereby facilitating validation without requiring additional DSA acquisitions during clinical imaging (which would require additional injection of contrast and additional x-ray exposure, thereby significantly increasing risk to the patient).

Each pixel in an annotated image encodes four values that we use to constrain 3D reconstructions; the distance d to the closest point on the projected centerlines; the radius r of the vessel at that point; the bolus arrival time t at that point; and v_y, a function of the bolus velocity described below. For this paper, these values were computed directly from the 3D models. However, each component could be derived from 2D DSA sequences by extracting centerlines and radii (Chapman et al., 2004; Frangi et al., 1998; Gao et al., 2017; Lu et al., 2016; Phellan and Forkert, 2017; Yaxley and Coleman, 2018; Zou et al., 2015) and bolus arrival times (Davis et al., 2013; Haouchine and Frisken, 2021; Platzer et al., 2008).

To define v_y, we first define the 2D projected bolus velocity, v for a point (x, y) on a 2D centerline as $v \equiv (v_x, v_y) = (dx/dt, dy/dt)$, where dx/dy is the slope of the 2D centerline at $(x,\ y)$ and dt is the instantaneous change of arrival times at $(x,\ y)$. For each line segment of the 2D centerline, v can be computed from the 2D positions and bolus arrival times of the segment endpoints. Because vessels generally do not lie parallel to a given view, v is different from the 3D bolus velocity and it is different in different views. However, when two 2D views share a common axis, as is typical in angiography systems used to acquire DSA, the component of v in the shared axis is the same in both views. Without loss of generality, we assume the shared axis is the y-axis of our 2D projection images (i.e., the bottom-to-top or *inferior-superior* axis for our chosen view directions). Thus, the projection of the same vessel point into two different views will have the same value of v_y. We make use of this fact to help constrain 3D reconstruction.

The simplest way to represent each 2D annotated image is as a 2D array of 4 floating point values: d, r, t, and v_y. However, this can be memory intensive and computational expensive for high resolution DSA images (e.g., 2048^2 pixels → 67 MB per image). There are many ways to reduce storage and computation times, e.g., by representing each value as a single byte instead of a floating point value, by only annotating images within a few pixels of vessel centerlines and/or by computing and storing the annotated image in a spatial data structure such as a quadtree (Frisken et al., 2000). We take advantage of the fact that our centerlines are stored as a list of line segments and represent annotated images as 2D arrays of integer values, where the value of each pixel is the index of the line segment closest to the pixel if the centerline is closer than a specified radius of interest R, or −1 if it is

farther than R from the pixel. Distances, radii and other values are computed on the fly as needed by our reconstruction algorithm. For the results presented in this paper, we used pixel dimensions 1 mm^2 and a radius of interest R = 5 mm for annotated images. We note that, because distances to centerlines are computed with floating point precision, this provides much higher resolution than a binary segmentation of vessel centerlines at the same pixel resolution (Frisken et al., 2000).

3. Theory and calculation

We present a volumetric reconstruction method, but we note that our approach could also be used to constrain model-based reconstruction. As described in the Background, others have reconstructed 3D vasculature from multiple 2D views by back projecting a distance field representation of 2D centerlines extracted from DSA images into 3D space. This approach can work when the vessel structure is relatively simple, and the number of projections is sufficient. However, with only two view directions, overlapping vessels and vessels that run nearly perpendicular to one of the view directions result in ghost structures that do not lie on centerlines of the true 3D vasculature (Fig. 6). With well-chosen view directions, simple structures, e.g., single vessels, short vessel segments or the larger coronary arteries, yield relatively few ghosts. In these situations, user input, vessel connectivity or an a priori model of vessel structure could be used to disambiguate the 3D reconstruction and eliminate ghosts. However, the amount of ghosting quickly increases with the complexity of the vasculature (Fig. 7). We address this problem by using additional metrics that can be derived directly from 2D DSA sequences (namely vessel radii, bolus arrival times and v_y) to constrain the volumetric reconstruction.

To generate 3D reconstructions from pairs of 2D annotated images, an image volume of size 512^3 with voxel dimensions $1mm^3$ was created. Each voxel was initialized to zero to indicate that the likelihood that the voxel contained a vessel centerline was zero. Then, for each voxel in the reconstruction volume, the voxel position was projected onto the annotated images using the same cone-beam projection geometry used to generate the 2D images. The annotation values (i.e., distance to the closest centerline point d, vessel radius r, bolus arrival time t, and velocity component v_y) were computed in each annotated image from pixel values surrounding the projected voxel using bilinear interpolation. Then the voxel value V, i.e., was computed as the product:

$$V = D(d_1, d_2) \times C(d_1, d_2, r_1, r_2, t_1, t_2, v_{y1}, v_{y2}), \tag{1}$$

where n_1 and n_2 indicate values for the variable n (i.e., d, r, t, v_y) computed from annotation image 1 and 2 respectively, D is a method for combining distance values and C is a confidence in the reconstructed distance based on variation in the radii, bolus arrival time and velocity components.

There are several possible methods for combining distance values. For our purposes, D should range from zero for points known to be far from the centerline to one for points

that, subject to vessel overlapping and reconstruction ambiguity, have a high likelihood of being at the centerline. We tested two commonly used methods: the average distance (2) and maximum distance (3):

$$D_{avg} = 1 - max((d_1 + d_2)/(2R), 1), \tag{2}$$

$$D_{max} = 1 - max((max(d_1, d_2))/R, 1), \tag{3}$$

Dividing by R scales the combined distance values to 1 at a distance R from the centerline. Clamping the scaled, combined distance values to 1 and subtracting the clamped values from 1 ensures that the output of both functions will be one at the centerline and zero where we are certain there is no centerline. We used (3) in the results presented in this paper, though both (2) and (3) produced similar results with significant ghosting when the confidence function is set to 1.0 (Figure 10, second row). The confidence function, C, applies constraints to the reconstruction by ensuring that the annotated vessel radii, bolus arrival times, and v_y values are similar at the projections of each voxel into the 2D annotated segmentations. We combine these constraints using the multiplicative confidence function C:

$$C = C_r(|r_1 - r_2|) \times C_t(|t_1 - t_2|) \times C_{vy}(|v_{y1} - v_{y1}|), \text{ where} \tag{4}$$

$$C_n(\left|\Delta n\right|) = \begin{cases} 1 \ for \ \Delta n < n_{min} \\ \frac{(\Delta n - n_{min})}{(n_{max} - n_{min})} \ for \ n_{min} < \Delta n < n_{max}, \\ 0 \ for \ \Delta n > n_{max} \end{cases} \tag{5}$$

where $|x|$ is absolute value of x As can be seen in (5), $C_n(n, \ n > 0)$ is a function whose output ranges linearly from 1.0 to 0.0 for n between $n_{\min}$ and $n_{\max}$ and is clamped to 1.0 for $n < n_{\min}$ and to 0.0 for $n > n_{\max}$. Using $n_{\min}$ and $n_{\max}$ instead of a single threshold reduces the dependency on the threshold used for Δn. We set $n_{\min}$ and $n_{\max}$ to 2% and 10% of the maximum radius, arrival time, and v_y value for each model, but results were not sensitive to $n_{\min}$ and $n_{\max}$ and these parameters are not critical for success.

3.1 Visualization

Reconstructed voxel values represent the likelihood that a voxel contains a vessel centerline. Likelihoods range from zero for points guaranteed to be further than R from a centerline to one for points where we have a high confidence that the point is on a centerline. A likelihood between zero and one indicates that the point may be less than R from a centerline but that our confidence is low that this point is not a ghost point, perhaps

due to overlapping vessels or a vessel that runs nearly perpendicular to one of the views. The reconstructed volume can be visualized using direct volume rendering or iso-surface rendering. In this paper, reconstructed volumes are rendered as semi-transparent iso-surfaces, where an iso-surface value of 0.6 was selected to illustrate regions of high likelihood. Iso-surface generation and visualization were performed using 3D Slicer, an open source platform for medical image processing and visualization (www.3dslicer.org, 2020).

4. Results and Discussion

Figs. 8 and 9 show examples of a fractal tree model and a BraVa model of a middle cerebral artery respectively with their corresponding annotated 2D images. Figure 10 compares reconstructions of the models (top row) from Fig. 8 and 9 using different constraints. The reconstructed volumes show a great deal of ghosting when no constraints are used during reconstruction (second row). Using any of the constraints that we propose (i.e., vessel radii, bolus arrival times or velocity component v_y) reduces the amount of ghosting and each constraint reduces the amount of ghosting differently, leaving behind different patches of ghosting. When all three constraints are combined, the result is nearly ghost free and the small remaining patches of ghosting generally lie far from true vessel centerlines. Most importantly, when the constraints are applied, the voxels where likelihood values are high lie mostly along true vessel centerlines. There are stretches along true vessel centerlines where the likelihood is small (< 0.6) due to overlapping vessles or vessels that run nearly perpendicular to one of the two projection views. However, these stretches are relatively short and could easily be combined during the third stage of our pipeline using vessel connectivity requirements to generate vessel models. While parameters used to weight the impact of the constraints in (5) were hand-tuned, our method is not particularly sensitive to these parameters. More careful hand tuning and/or deep-learning methods for setting parameters could improve our results. In addition, other confidence functions could be considered.

We applied our method to a fractal tree with three different levels of branching and the vascular models of the BraVa dataset. The BraVa dataset contains 6 circulations (left and right anterior, middle and posterior cerebral arteries) for 61 subjects. For each of these 366 models, we generated annotated 2D images, reconstructed volumes and measured the amount of ghosting and the coverage of the vessel centerlines for each reconstructed volume. These results are summarized in Table I. Table I confirms the visual results of Figs. 6 and 7, which show that the amount of ghosting increases with complexity of the fractal tree. It also confirms the results of Fig. 10 which shows that our method for constraining the 3D reconstruction of cerebral vasculature reduces the amount of ghosting by 99%, thereby greatly simplifying vessel model generation in stage 3 of our pipeline. Overlapping vessels and vessels that run nearly parallel to one of the 2D views result in likelihood values of less than 0.4 for 25% of true centerline voxels.

4.1 Discussion

While these results are promising, there is still much work to be done. This method relies on vessel centerlines segmented from 2D DSA that are annotated with vessel radii and

bolus arrival times. Our next steps will be developing and testing algorithms to perform this annotated segmentation. We plan to leverage the significant body of literature on segmenting vessel centerlines and radii (e.g., (Chapman et al., 2004; Frangi et al., 1998; Gao et al., 2017; Lu et al., 2016; Phellan and Forkert, 2017; Yaxley and Coleman, 2018; Zou et al., 2015)) and recent work on detecting bolus arrival times in 2D DSA sequences (Davis et al., 2013; Haouchine and Frisken, 2021; Platzer et al., 2008).

The work presented here assumes perfectly annotated segmentations in order to focus on how the proposed constraints could reduce ghosting artifacts in the volumetric reconstruction under optimal conditions. We have not addressed image artifacts present in real-world clinical data, including noise and differences in x-ray attenuation and scattering in the two DSA image sequences. Rather than trying to simulate the effects of these image artifacts on ghosting per se, we will address them using actual clinical data when we develop and test algorithms for performing annotated segmentation. We will then explore the impact of imperfect segmentation from clinical data on ghosting in volumetric reconstruction.

Since we intend to use this system intraoperatively, it is important to consider the speed of the proposed approach. Methods described in this paper were implemented in C++ and run on an off-the-shelf desktop system with a high-end graphics processor (Dell XPS 8940, i7–11700 processor, NVIDIA GeForce GTX 1660). While the implementation was not optimized for speed, the annotated images of Figs. 8 and 9 were generated in less than a second using the stroke rendering method described in (Frisken, 2008), and the volumes of Figure 10 were reconstructed in a few seconds. These times are well within requirements for intraoperative clinical use.

Finally, we plan to generate 3D models of the vasculature from the volumetric representation output from stage 2 so that we use the models in for simulating motion of a bolus of contrast agent through the vessels. Our constrained reconstruction method greatly reduces ghosting artifacts (Fig. 10) but also results in gaps in vessel centerlines where there is structural ambiguity in the two views. In future work, we will adapt existing approaches to generate models of the vascular structure from the output of stage 2. We plan to investigate the use of vessel connectivity and models of vessel growth and propagation as well as vessel radii and bolus arrival times to guide and constrain model generation.

5. Conclusions

We have presented a new method for reconstructing a 3D representation of blood vessels from two 2D DSA image sequences. Unlike previous approaches which constrain this ill-defined problem either by limiting the application to single curves or relatively simple vessel structures or by using multiple 2D images and/or a prior 3D model of the vasculature (e.g., from MRA or CTA), our method constrains the 3D reconstruction using temporal and structural data that can be derived directly from the 2D DSA sequences. Specifically, we use 2D vessel centerlines, vessel radii and data about the timing of contrast agent as it moves through the vessels during image acquisition.

This work provides a solution for one stage of a three-stage pipeline and is an important step towards our goal of generating 3D images of cerebral vasculature with a spatial and temporal resolution approaching that of 2D DSA from a single pair of 2D DSA sequences acquired on a biplane angiography system. Planned future work will address the other two stages of the pipeline, validate the entire pipeline on clinical data, and build a system that integrates the three stages into a single software system that is fast and robust enough to be used for preoperative planning and intraoperative guidance.

Acknowledgements

This work was funded by a research pilot grant from the Department of Radiology at Brigham and Women's Hospital.

References

Benes V, Bradáč O, 2017. Brain Arteriovenous Malformations : Pathogenesis, Epidemiology, Diagnosis, Treatment and Outcome. Springer, Cham, SWITZERLAND.

Berthilsson R, Astrom K, 1997. Reconstruction of 3D-curves from 2D-images using affine shape methods for curves, Proceedings of IEEE Computer Society Conference on Computer Vision and Pattern Recognition, pp. 476–481.

Blondel C, Vaillant R, Malandain G, Ayache N, 2004. 3D tomographic reconstruction of coronary arteries using a precomputed 4D motion field. Phys Med Biol 49, 2197–2208. [PubMed: 15248572]

Bullitt E, Liu A, Pizer SM, 1997. Three-dimensional reconstruction of curves from pairs of projection views in the presence of error. I. Algorithms. Med Phys 24, 1671–1678. [PubMed: 9394273]

Cai Y, Su Z, Li Z, Sun R, Liu X, Zhao Y, 2011. Two-view curve reconstruction based on the snake model. Journal of Computational and Applied Mathematics 236, 631–639.

Cardenes R, Novikov A, Gunn J, Hose R, Frangi AF, 2012. 3D reconstruction of coronary arteries from rotational X-ray angiography, 2012 9th IEEE International Symposium on Biomedical Imaging (ISBI), pp. 618–621.

Chapman BE, Stapelton JO, Parker DL, 2004. Intracranial vessel segmentation from time-of-flight MRA using pre-processing of the MIP Z-buffer: accuracy of the ZBS algorithm. Med Image Anal 8, 113–126. [PubMed: 15063861]

Chen D, Deng J, Xie X, Nithiarasu P, Smith D, 2013. Efficient Reconstruction of Coronary Vessels from 2D Angiography, In: Nithiarasu P, Lohner R. (Eds.), 3rd International Conference on Computational and Mathematical Biomedical Engineering, Hng Kong.

Chen SJ, Carroll JD, 2000. 3-D reconstruction of coronary arterial tree to optimize angiographic visualization. IEEE Transactions on Medical Imagin 19, 318–336.

Çimen S, Gooya A, Grass M, Frangi AF, 2016. Reconstruction of coronary arteries from X-ray angiography: A review. Medical Image Analysis 32, 46–68. [PubMed: 27054277]

Copeland AD, Mangoubi R, Desai MN, Mitter SK, Malek AM, 2010. Spatio-temporal data fusion for 3D+T image reconstruction in cerebral angiography. IEEE Trans Med Imaging 29, 1238–1251. [PubMed: 20172817]

Davis B, Royalty K, Kowarschik M, Rohkohl C, Oberstar E, Aagaard-Kienitz B, Niemann D, Ozkan O, Strother C, Mistretta C, 2013. 4D digital subtraction angiography: implementation and demonstration of feasibility. Am J Neuroradiol 34, 1914–1921. [PubMed: 23620072]

Delmas C, Berger M, Kerrien E, Riddell C, Trousset Y, Anxionnat R, Bracard S, 2015. Three-dimensional curvilinear device reconstruction from two fluoroscopic views, Proc.SPIE.

Diestel W, Moeller M, 2003–2012. Arbaro, http://arbaro.sourceforge.net/.

Fang H, Yang J, Zhu J, Ai D, Huang Y, Jiang Y, Song H, Wang Y, 2018. Greedy Graph Searching for Vascular Tracking in Angiographic Image Sequences. IEEE Transactions on Circuits and Systems for Video Technology 30, 1466–1480.

Feldkamp LA, Davis LC, Kress JW, 1984. Practical cone-beam algorithm. J. Opt. Soc. Am. A 1, 612–619.

Frangi AF, Niessen WJ, Vincken KL, Viergever MA, 1998. Multiscale vessel enhancement filtering, In: Wells WM, Colchester A, Delp S. (Eds.), Medical Image Computing and Computer-Assisted Intervention — MICCAI'98. Springer Berlin Heidelberg, Berlin, Heidelberg, pp. 130–137.

Frisken S, Perry R, Rockwood A, Jones TR, 2000. Adaptively Sampled Distance Fields: a general representation of shape for computer graphics. ACM SIGGRAPH, 249–254.

Frisken S. 2008, Efficient Curve Fitting, Journal of Graphics GPU and Game Tools. 13(2):37–54.

Galassi F, Alkhalil M, Lee R, Martindale P, Kharbanda RK, Channon KM, Grau V, Choudhury RP, 2018. 3D reconstruction of coronary arteries from 2D angiographic projections using non-uniform rational basis splines (NURBS) for accurate modelling of coronary stenoses. PLoS One 13, e0190650-e0190650.

Gao S, van 't Klooster R, Kitslaar PH, Coolen BF, van den Berg AM, Smits LP, Shahzad R, Shamonin DP, de Koning PJH, Nederveen AJ, van der Geest RJ, 2017. Learning-based automated segmentation of the carotid artery vessel wall in dual-sequence MRI using subdivision surface fitting. Med. Phys 44, 5244–5259. [PubMed: 28715090]

Garcia J, 2013. Three-Dimensional Imaging for Coronary Interventions: Techniques and technologies for more accurate vessel views. Cardiac Interventions Today January/February 2013, 55–60.

Gauvrit JY, Leclerc X, Oppenheim C, Munier T, Trystram D, Rachdi H, Nataf F, Pruvo JP, Meder JF, 2005. Three-dimensional dynamic MR digital subtraction angiography using sensitivity encoding for the evaluation of intracranial arteriovenous malformations: a preliminary study. Am. J. Neuroradiol 26, 1525–1531. [PubMed: 15956525]

Griffiths PD, Hoggard N, Warren DJ, Wilkinson ID, Anderson B, Romanowski CA, 2000. Brain arteriovenous malformations: assessment with dynamic MR digital subtraction angiography. Am. J. Neuroradiol 21, 1892–1899. [PubMed: 11110543]

Grist TM, Mistretta CA, Strother CM, Turski PA, 2012. Time-resolved angiography: Past, present, and future. J. Magn Reson Imaging 36, 1273–1286. [PubMed: 22566099]

Haouchine N, Frisken S, 2021. Estimation of High Framerate Digital Subtraction Angiography Sequences at Low Radiation Dose, MICCAI.

Henri CJ, Peters TM, 1996. Three-dimensional reconstruction of vascular trees. Theory and methodology. Med. Phys 23, 197–204. http://cng.gmu.edu/brava, 2020. [PubMed: 8668100]

Ide S, Hirai T, Morioka M, Kai Y, Yano S, Kawano T, Tochihara S, Shigematsu Y, Uetani H, Murakami Y, Watanabe K, Yamashita Y, 2012. Usefulness of 3D DSA-MR fusion imaging in the pretreatment evaluation of brain arteriovenous malformations. Academic Radiology 19, 1345–1352. [PubMed: 22951112]

Jandt U, Schäfer D, Grass M, Rasche V, 2009. Automatic generation of 3D coronary artery centerlines using rotational X-ray angiography. Med Image Anal 13, 846–858. [PubMed: 19713148]

Kalani M, Yashar S, 2015. Neurovascular surgery. Thieme Medical Publishers Inc.

Lawton MT, Lang MJ, 2019. The future of open vascular neurosurgery: perspectives on cavernous malformations, AVMs, and bypasses for complex aneurysms. Journal of Neurosurgery JNS 130, 1409–1425.

Lee NY, Kim GY, Choi HI, 2007. 3D Modeling of the Vessels from X-Ray Angiography, In: Duffy VG (Ed.), Digital Human Modeling. Springer Berlin Heidelberg, Berlin, Heidelberg, pp. 646–654.

Li J, Cohen L, 2011. Reconstruction of 3D Tubular Structures from Cone-Beam Projections, 2011 IEEE Int. Symp. Biomed. Imaging. IEEE, Chicago, Il, pp. 1162–1166.

Liao R, Luc D, Sun Y, Kirchberg K, 2010. 3-D reconstruction of the coronary artery tree from multiple views of a rotational X-ray angiography. Int J Cardiovasc Imaging 26, 733–749. [PubMed: 19885737]

Lu P, Xia J, Li Z, Xiong J, Yang J, Zhou S, Wang L, Chen M, Wang C, 2016. A vessel segmentation method for multi-modality angiographic images based on multi-scale filtering and statistical models. BioMedical Engineering OnLine 15.

Mai F, Hung Y, 2010. 3D Curves Reconstruction from Multiple Images, International Conference on Digital Image Computing: Techniques and Applications, pp. 462–467.

Martin T, Montes J, Bazin JC, Popa T, 2014. Topology-aware reconstruction of thin tubular structures. SIGGRAPH Asia 2014 Technical Briefs, SA 2014.

Matsumoto M, Kodama N, Endo Y, Sakuma J, Suzuki K, Sasaki T, Murakami K, Suzuki K, Katakura T, Shishido F, 2007. Dynamic 3D-CT angiography. Am J Neuroradiol 28, 299–304. [PubMed: 17296999]

Merle AB, Finet G, Lienard J, Magnin IE, 1998. 3D reconstruction of the deformable coronary tree skeleton from two X-ray angiographic views, Computers in Cardiology 1998. Vol. 25 (Cat. No.98CH36292), pp. 757–760.

Orth RC, Wallace MJ, Kuo MD, 2008. C-arm cone-beam CT: general principles and technical considerations for use in interventional radiology. J Vasc Interv Radiol 19, 814–820. [PubMed: 18503894]

Oueslati C, Mabrouk S, Ghorbel F, Bedoui MH, 2018. 3D Reconstruction of Coronary Arteries from Rotational X-Ray Angiography, IEEE Int. Symp. Biomed Imaging, Barcelona, pp. 618–621.

Phellan R, Forkert ND, 2017. Comparison of vessel enhancement algorithms applied to Time-of-Flight MRA images for cerebrovascular segmentation. Medical physics 44.

Platzer E-S, Deinzer F, Paulus D, Denzler J, 2008. 3D Blood Flow Reconstruction from 2D Angiograms, In: Tolxdorff T, Braun J, Deserno TM, Horsch A, Handels H, Meinzer H-P (Eds.), Bildverarbeitung für die Medizin 2008. Springer Berlin Heidelberg, Berlin, Heidelberg, pp. 288–292.

Rolston J, Han S, Lau C, Berger M, Parsa A, 2013. Frequency and predictors of complications in neurological surgery: national trends from 2006 to 2011. Journal of neurosurgery 120.

Saini D, Kumar S, Gulati T, 2015. NURBS-based Geometric Inverse Reconstruction of Free-form Shapes. Journal of King Saud University - Computer and Information Sciences 29.

Schmitt H, Grass M, Rasche V, Schramm O, Haehnel S, Sartor K, 2002. An X-ray-based method for the determination of the contrast agent propagation in 3-D vessel structures. IEEE Trans Med Imaging 21, 251–262. [PubMed: 11989849]

Spiegel M, Redel T, Struffert T, Hornegger J, Doerfler A, 2011. A 2D driven 3D vessel segmentation algorithm for 3D digital subtraction angiography data. Physics in medicine and biology 56, 6401–6419. [PubMed: 21908904]

Tran PB, 2017. 3D Reconstruction of Coronary Arteries Using Feldkamp-Davis-Kress Algorithm, Information Technology. Ecole de Technologie Superieure University Du Quebec, Montreal, Canada, p. 65.

Tsuchiya K, Katase S, Yoshino A, Hachiya J, 2000. MR digital subtraction angiography of cerebral arteriovenous malformations. Am J Neuroradiol 21, 707–711. [PubMed: 10782782]

Vardhan M, Gounley J, Chen SJ, Kahn AM, Leopold JA, Randles A, 2019. The importance of side branches in modeling 3D hemodynamics from angiograms for patients with coronary artery disease. Scientific Reports 9.

Vassallo R, Kasuya H, Lo B, Peters T, Xiao Y, 2018. Augmented reality guidance in cerebrovascular surgery using microscopic video enhancement. Healthcare Technology Letters 5.

Wachter I, 2009. 3D reconstruction of cerebral blood flow and vessel morphology from x-ray rotational angiography. Doctoral thesis, UCL (University College London).

Wacker E-S, Deinzer F, Paulus D, Denzler J, 2008. 3D Blood Flow Reconstruction from 2D Angiograms.

Weber J, Penn J, 1995. Creation and rendering of realistic trees. ACM SIGGRAPH 22, 119–128. www.3dslicer.org, 2020.

Xiao S, Bresler Y, Munson DC, 2003. Fast Feldkamp algorithm for cone-beam computer tomography, Proceedings 2003 International Conference on Image Processing (Cat. No.03CH37429), pp. II–819.

Yaxley KL, Coleman PM, 2018. Deep convolutional neural networks for automated vessel segmentation of cerebral MR angiograms, The Royal Australian and New Zealand College of Radiologists.

Zhang Q, Zhang Z, Yang J, Sun Q, Luo Y, Shan T, Zhang H, Han J, Liang C, Pan W, Gu C, Mao G, Xu R, 2016. CBCT-based 3D MRA and angiographic image fusion and MRA image navigation for neuro interventions. Medicine (Baltimore) 95, e4358. [PubMed: 27512846]

Zifan A, Liatsis P, 2016. Patient-Specific Computational Models of Coronary Arteries Using Monoplane X-Ray Angiograms. Comput Math Methods Med.

Zifan A, Liatsis P, Kantartzis P, Gavaises M, Karcanias N, Katritsis DG, 2008. Automatic 3D Reconstruction of Coronary Artery Centerlines from Monoplane X-ray Angiogram Images. International Journal of Biological and Medical Sciences 2, 105–110.

Ziyeh S, Strecker R, Berlis A, Weber J, Klisch J, Mader I, 2005. Dynamic 3D MR angiography of intra- and extracranial vascular malformations at 3T: a technical note. Am J Neuroradiol 26, 3. [PubMed: 15661689]

Zou H, Zhang W, Wang Q, 2015. An improved cerebral vessel extraction method for MRA images. Biomed Mater Eng, S1231–S1240. [PubMed: 26405882]

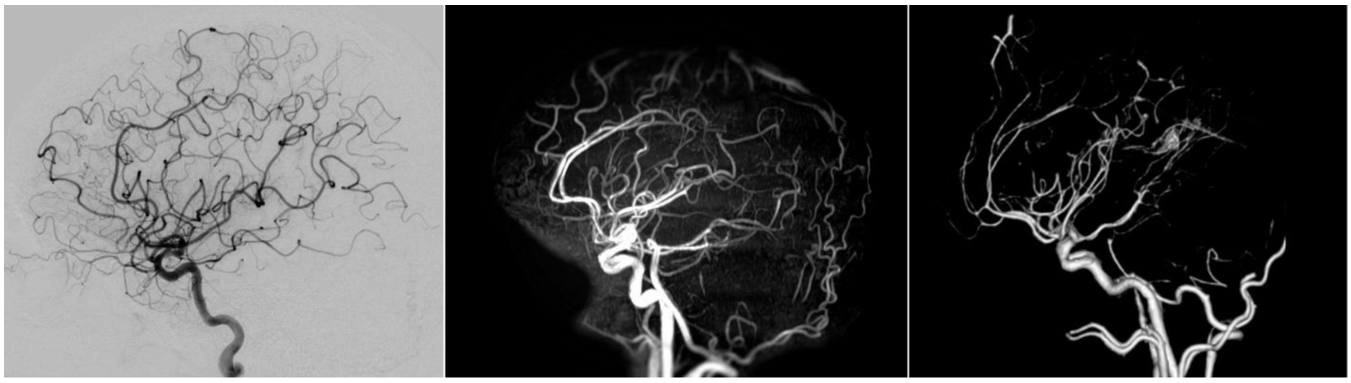

Figure 1.

Cerebral vasculature imaging of a healthy subject. Left: 2D DSA near the end of the arterial phase. Center: maximum intensity projection from MRA. Right: 3D model generated from CTA. MRA and CTA provide lower spatial resolution than DSA.

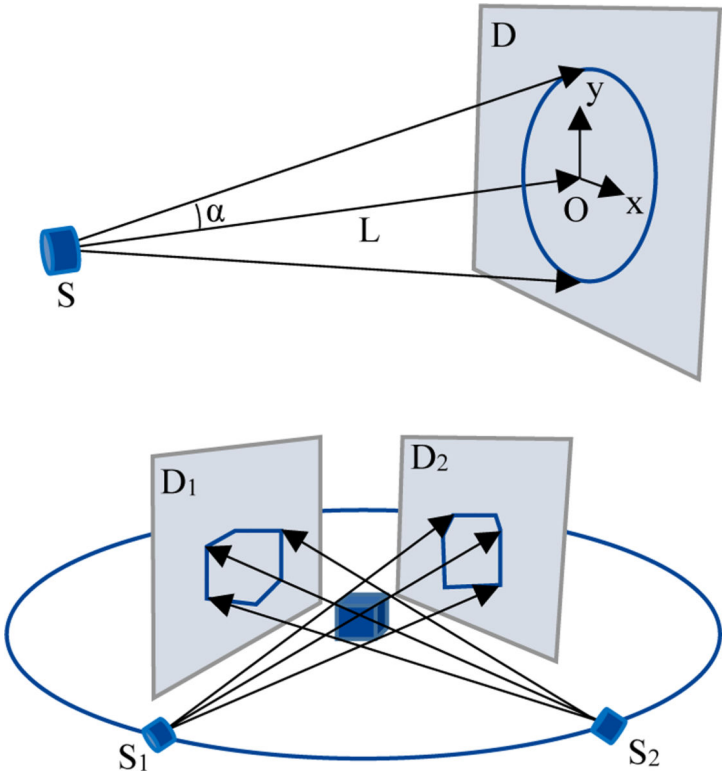

Figure 2.

Cone beam projection geometry typical in DSA angiography systems. Top: X-rays are projected from source S located at a distance L from the detector D about a central axis that intersects the detector at right angles at origin O. Image (x, y) coordinates are centered at O with y defined the *up vector*. Bottom: In biplane angiography, two sources (S_1 and S_2) and two detectors (D_1 and D_2), typically at right angles, can be used to produce two DSA sequences simultaneously. The sources and detectors are mounted so they can be rotated on a circular arc about the patient to obtain multiple sequences (e.g., for rotational angiography).

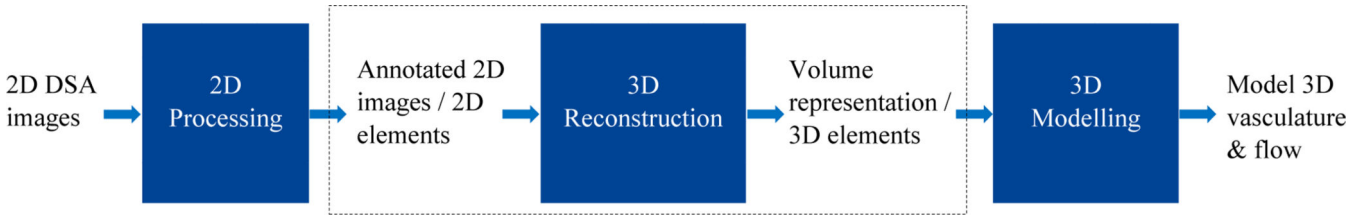

Figure 3.

The three stages of our full pipeline: 1) process each 2D DSA sequence to generate an annotated 2D image or an annotated set of 2D model elements; 2) reconstruct a volume representation from the annotated images/elements; and 3) generate a 3D model of the vasculature and simulate dynamic flow of contrast agent. This paper provides and evaluates a new algorithm for stage 2.

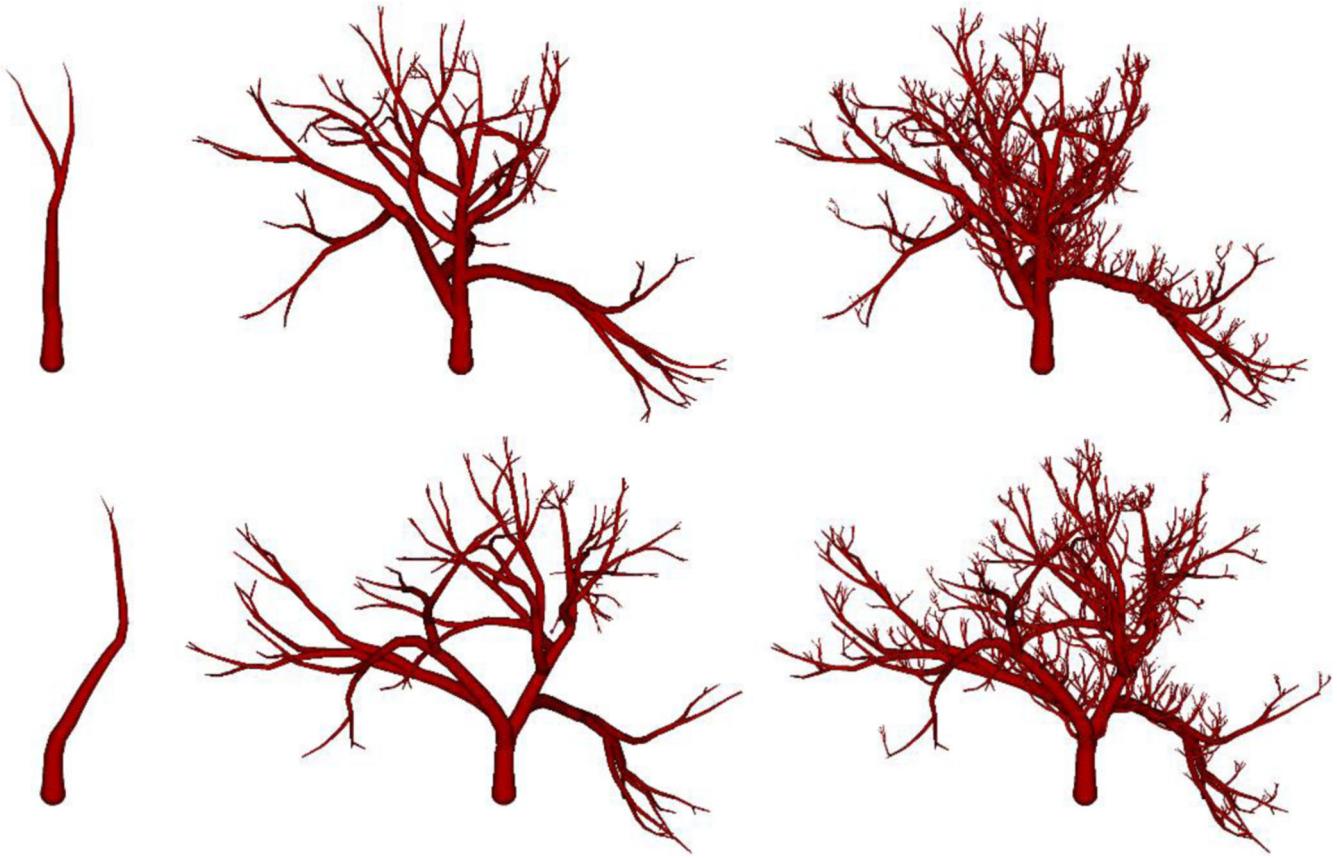

Figure 4.

Fractal trees used for testing. Fractal trees have the advantage that tree shape, branching pattern, average branch length and radius and number of branching level scan be controlled. Left: two orthogonal views of a fractal tree phantom with one branching level. Center: the same views of the phantom with two branching levels. Right: the same tree with three branching levels.

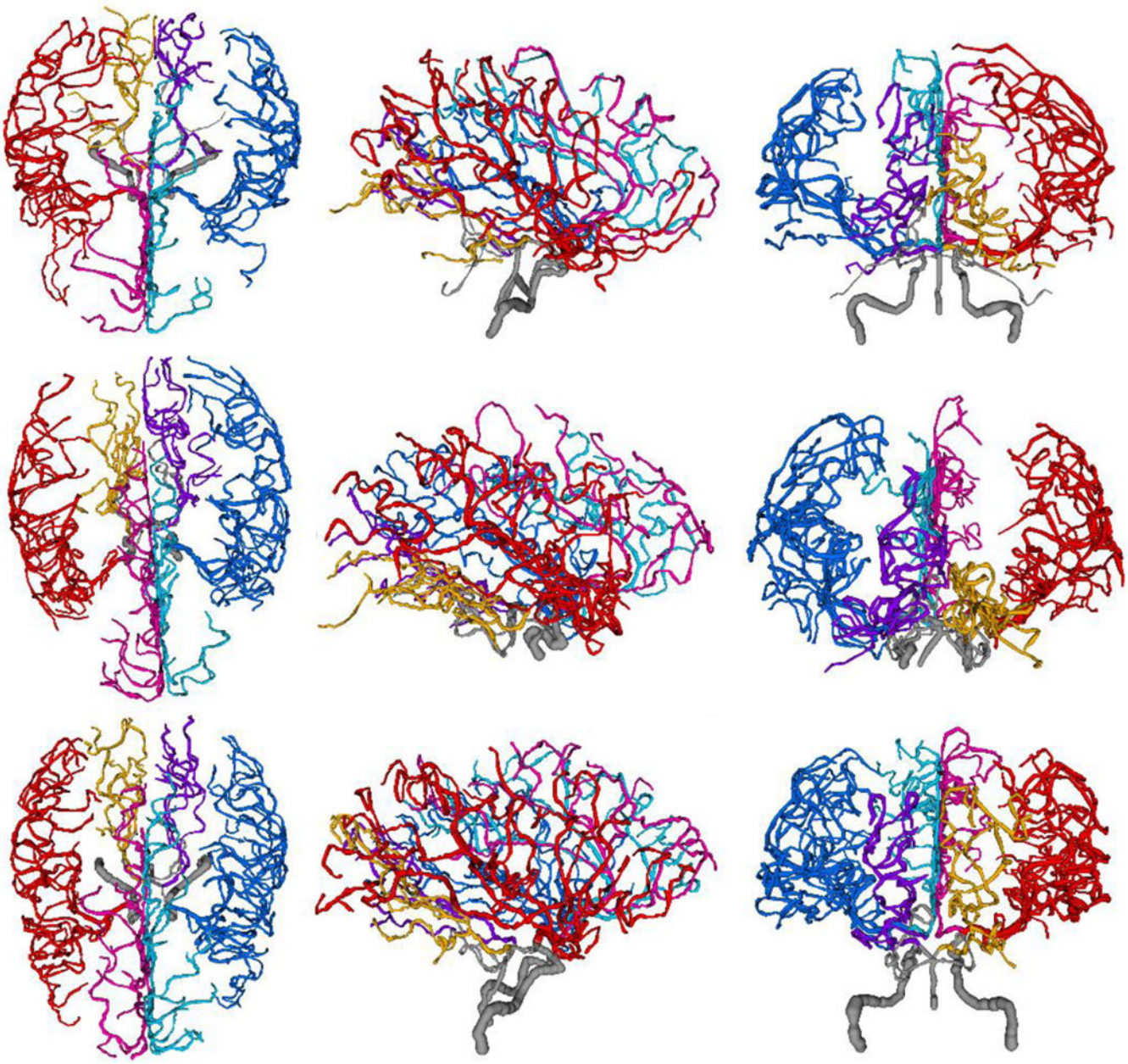

Figure 5.

Examples of 3D vessel phantoms of brain arterial trees generated from The Brain Vasculature (BraVa) database [60] which stores centerlines and radii of the left and right anterior, middle and posterior cerebral arteries from MRA of 61 subjects.

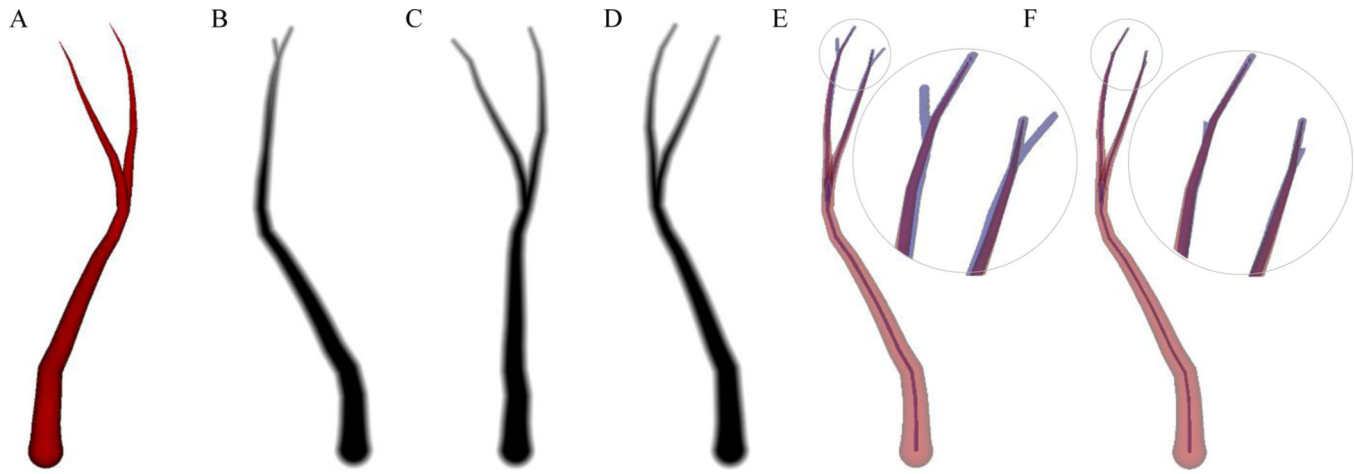

Figure 6.

A) Simple fractal tree phantom with one level of branching. B), C) Projections of the phantom onto two detector planes at 90 degrees to each other with B) illustrating overlapping of the smaller branches. D) A projection at 45 degrees between B and C. E) 3D reconstruction using only B) and C) shows ghosting (transparent blue ghost branches in the expanded circle). F) Ghosting is reduced when the third projection of C) is also used in the 3D reconstruction.

Figure 7.

Left to Right: Fractal tree phantom with two levels of branching, projections of the phantom onto two detector planes at 90 degrees to each other, and the 3D reconstruction viewed from the one of the projection directions and from an oblique direction. When the reconstruction is viewed from one of the two view directions, it looks perfect (blue centerlines are well aligned with the centerlines of the original tree model). However, as shown in the oblique view of the far right, overlapping vessels in the two views lead to large amounts of ghosting in the reconstructed model.

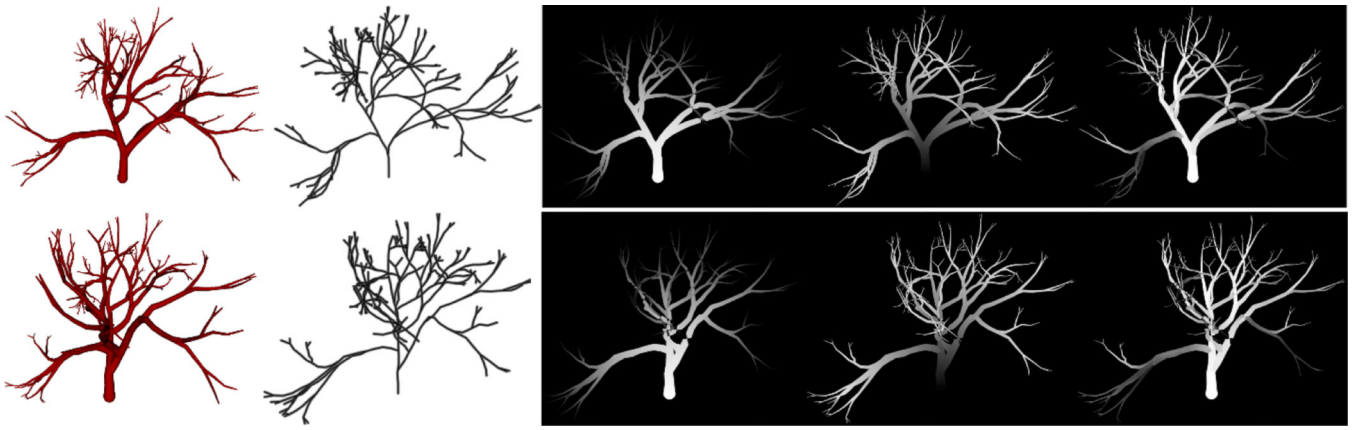

Figure 8.

Annotations of a fractal tree phantom. Top row: lateral view. Bottom row: front-to-back view of the fractal tree with two branching levels. The two left images show the 3D model and the projected centerlines. The three right images, left to right, show annotations of the vessel radii, bolus arrival time, and v_y encoded as grey scale values.

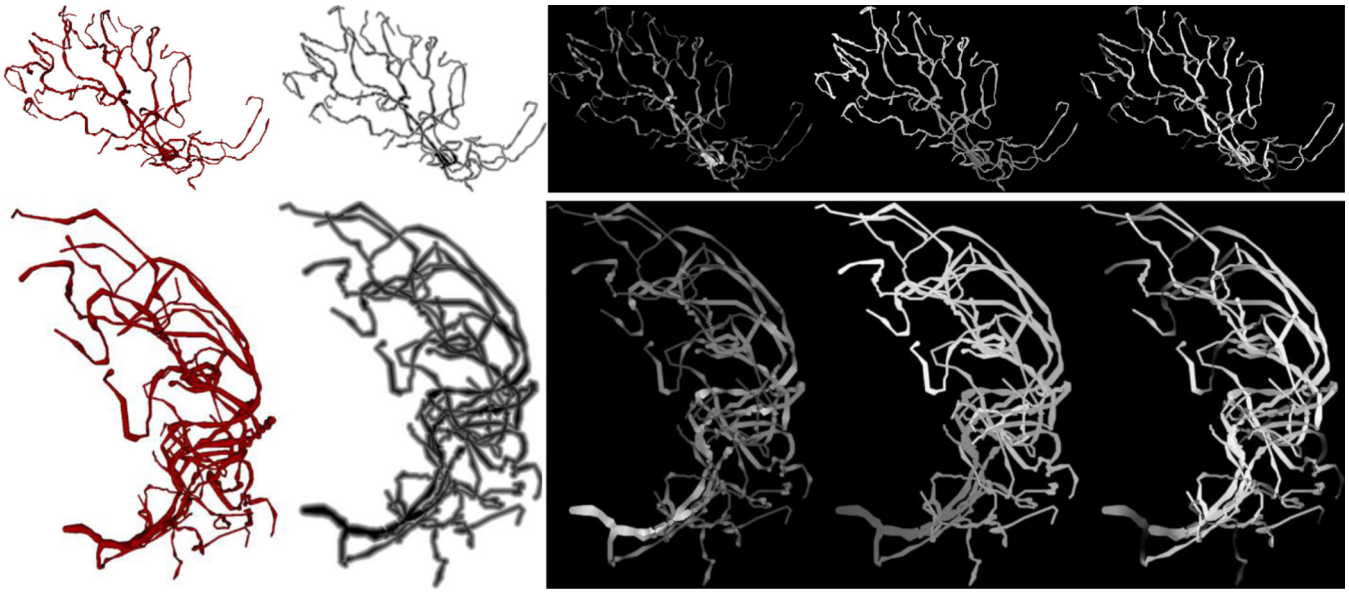

Figure 9.

Annotations of a BraVa vascular model. Top row: lateral view. Bottom row: front-to-back view of a phantom of the middle cerebral artery from a BraVa model. The two left images show the 3D model and the projected centerlines. The three right images, left to right, show annotations of the vessel radii, bolus arrival time, and v_y encoded as grey scale values.

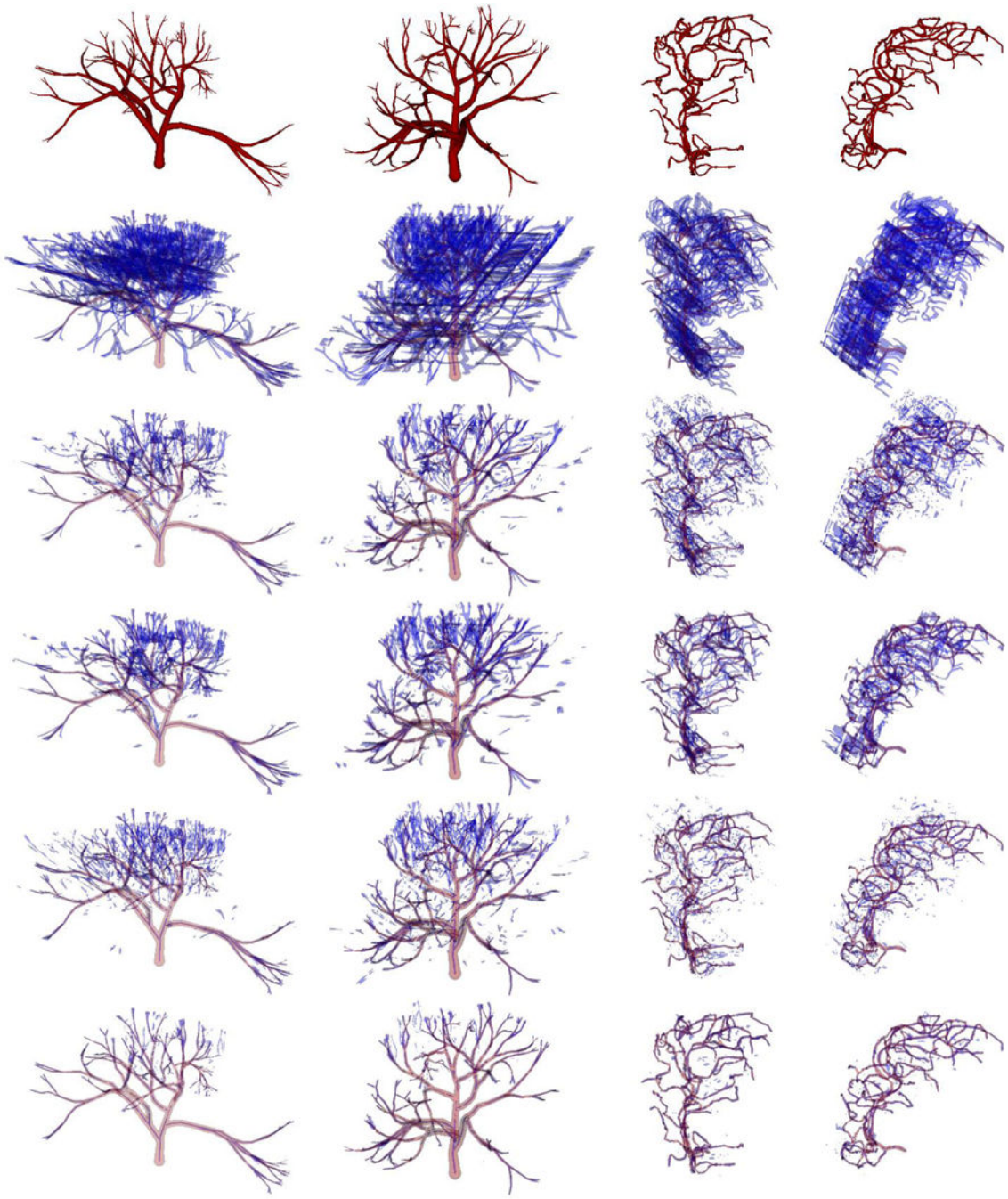

Figure 10.

Fractal tree phantom (left two columns) and a phantom of right middle carotid artery (right two columns) from oblique views showing ghosting. Each row (top to bottom) shows: a 3D model of the phantom; volume reconstruction with no constraints; volume reconstruction constrained by vessel radii; volume reconstruction constrained by bolus arrival times; volume reconstruction constrained by v_y; and volume reconstruction constrained by all three constraints.

TABLE I

NUMERICAL RESULTS

Data	# of ghost voxels in unconstrained data	% reduction in # of ghost voxels using proposed method	# actual centerline voxels	% centerline voxels in reconstruction with likelihood > 0.4
Fractal trees				
1 branch level	2,306	85.43	1838	100
2 branch levels	1,344,454	97.61	19,235	87.03
3 branch levels	4,513,565	95.34	65,629	56.38
BraVa models				
Anterior cerebral artery	216,404 +/− 83,533	99.35 +/− 0.24	6779 +/− 1444	74.37 +/− 5.93
Middle cerebral artery	487,660 +/− 403,142	99.25 +/− 0.34	9142 +/− 5480	74.44 +/− 7.14
Posterior cerebral artery	454,240 +/− 382,475	99.24 +/− 0.29	8901 +/− 5379	74.89 +/− 7.12

Numerical results show 1) for fractal tree models (Fig. 4), the number of ghost voxels (and the number of centerline voxels) increases with branching complexity and 2) for the BraVa models of cerebral vasculature, the number of ghost voxels varied quite a lot between models due to differences in model complexity. However, in all cases, the number of ghost voxels was reduced by 99% by using our constrained reconstruction instead of an unconstrained reconstruction while 75% of the centerline voxels were assigned a vessel likeliness > 0.4 even with a great deal of vessel overlap in the 2D image sequences.